LA-UR- 08-5466

Approved for public release;
distribution is unlimited.

Title:	Multivariate Analysis of Remote LIBS Spectra Using Partial Least Squares, Principal Component Analysies, and Related Techniques
Author(s):	Samuel M. Clegg Elizabeth Sklute M. Darby Dyar James E. Barefield Roger C. Wiens
Intended for:	Spectrochimica acta. Part B, Atomic spectroscopy

Los Alamos
NATIONAL LABORATORY
EST. 1943

Form 836 (7/06)

Multivariate Analysis of Remote LIBS Spectra Using Partial Least Squares, Principal Component Analysies, and Related Techniques

Samuel M. Clegg[a,*], Elizabeth Sklute[b], M. Darby Dyar[b], James E. Barefield[a], and Roger C. Wiens[c]

[a] Chemistry Division, Los Alamos National Laboratory, Los Alamos, NM 87544
[b] Mount Holyoke College, South Hadley, Massachusetts 01075
[c] International, Space & Response Division , Los Alamos National Laboratory, Los Alamos, NM 87544

Abstract

Quantitative analysis with LIBS traditionally employs calibration curves that are complicated by the chemical matrix effects. These chemical matrix effects influence the LIBS plasma and the ratio of elemental composition to elemental emission line intensity. Consequently, LIBS calibration typically requires a priori knowledge of the unknown, in order for a series of calibration standards similar to the unknown to be employed. In this paper, three new Multivariate Analysis (MVA) techniques are employed to analyze the LIBS spectra of 18 disparate igneous and highly-metamorphosed rock samples. Partial Least Squares (PLS) analysis is used to generate a calibration model from which unknown samples can be analyzed. Principal Components Analysis (PCA) and Soft Independent Modeling of Class Analogy (SIMCA) are employed to generate a model and predict the rock type of the samples. These MVA techniques appear to exploit the matrix effects associated with the chemistries of these 18 samples.

* Corresponding Author
E-mail address: sclegg@lanl.gov
LA-UR-07-5923

1. Introduction

Quantitative analysis with laser-induced breakdown spectroscopy (LIBS) is complicated by chemical matrix effects. Here we define chemical matrix effects as chemical properties of the material that influence the ratio of a given emission line to the abundance of the element producing that line. Chemical matrix effects are directly related to the elemental and molecular composition of the sample and ubiquitously perturb the LIBS plasma. They are related to the relative abundances of neutral and ionized species within the plasma, collisional interactions within the plasma, laser-to-sample coupling efficiency, and self absorption.[1-8] Minor or trace elements in the sample can cause chemical matrix effects on major element emission lines.[2, 9] Local atmospheric composition and pressure also significantly influence LIBS plasma intensity because the local atmosphere and the breakdown products from the atmospheric species interact with the ablated surface material in the plasma.

Many approaches have been developed to compensate for the chemical matrix effects and thereby to extract more quantitative elemental concentrations from LIBS spectra. In the traditional analytical chemistry approaches, the elemental peak heights or areas are extracted from spectra of unknowns and standards.[10] The standards' data are used to generate calibration curves for each element at one or more emission lines, which can then be used to interpret data from the unknowns. For best results, the calibration standards generally must have similar chemistries to the unknown samples, thus requiring a priori knowledge of the samples.[10, 11] Even when the unknown samples are chemically similar to the calibration set, such calibration data may be more scattered than desired for an accurate and precise quantitative analysis.

Several normalization methods have been employed to compensate for these matrix effects. Thompson et al. normalized their LIBS spectra to the total integrated emission intensity to compensate for the matrix effects as well as shot-to-shot fluctuations in the experiment.[10] Bolger employed the same approach to compensate for plasma variations due to sample surface geometry.[12] Another approach involves normalization of the elemental peak height or area to an internal spectral feature that should be sensitive to spectral changes related to the chemical matrix effects. Eppler et al. explored the chemical matrix effect of sand doped with Pb and Ba, and normalized the Pb (405.7nm) and Ba (233.5nm) peaks with both C (247.8nm) and Si (243.5nm).[6] Because the same sand samples were doped, the C and Si LIBS response should remain constant.

Calibration-free LIBS (CF-LIBS) is another quantitative analysis technique employed to compensate for matrix effects and increase the quantitative statistical certainty.[1, 11, 13-16] The CF-LIBS approach attempts to extract quantitative elemental abundance through a plasma physics model without the need for generating calibration curves. The model assumes that a state of Local Thermal Equilibrium (LTE) exists and that the plasma temperature described by the LTE is accurately extracted from the spectrum. It also assumes that the plasma is optically thin, despite the fact that self-absorption is known to be a LIBS complication.[1, 3] The integrated emission intensity is calculated assuming a Boltzmann distribution at the LTE temperature.

Finally, Salle et al. completed a comparative study of three different analysis techniques.[11] Their first method used a single reference sample and, assuming all major elements were detected, scaled the predicted concentrations such that the composition of the sample sums to 100%. Their second method involved normalizing the emission intensities to a

single spectral feature, such as the oxygen emission line at 777 nm. This line was a particularly good selection for that study because the samples were primarily oxides and the atmosphere was 7 Torr CO_2; thus this emission line should be representative of fluctuations in the experiment. CF-LIBS was the final analysis method tested. Among the three tested, normalization to the O lines appeared to be the best statistically.

This paper focuses on a newer, promising method for LIBS data interpretation using multivariate analysis (MVA) to extract quantitative elemental compositions and determine the likely rock-type or sample classification. Fundamentally, MVA is a mathematical and statistical approach to analyzing complex systems.[17, 18] LIBS spectra tend to be very complex and contain much information that is ignored by univariate techniques. In recent years, two variations of MVA have been used to analyze LIBS spectra. Martin et al. used Partial Least Squares (PLS) to create a calibration model and extract quantitative concentrations of elements uses in wood preservatives, including Cu, Zn, and As.[19] Principal Components Analysis (PCA) was also employed to qualitatively distinguish samples treated with different preservatives. Recently, Munson et al. used LIBS to probe bacterial spores, molds, pollens, and nerve agent simulants and employed PCA on the LIBS spectra to cluster the samples.[20] Partial Least Squares Regression (PLSR) has also been used to calibrate and quantitatively analyze the chromium concentration in soil samples.[21] Finally, Sirven et al. employed PCA, SIMCA and Partial Least Squares, Discriminant Analysis (PLS-DA) to predictively identify six igneous rock-types. They were successful at correctly classifying the samples 85.9% with PLS-DA alone and 100% with a combination of PLS-DA and SIMCA.

Remote LIBS research is a rapidly growing sub-field in which samples are located at distances up to tens of meters from the instrument. Remote LIBS instruments have been developed and tested on a wide range of samples including planetary science[10, 14, 16, 22, 23] and detection of high explosives. A recent review specifically of remote LIBS work was provided by Salle et al. that describes the current state of the art.[24] Remote LIBS instruments like ChemCam typically require specific design characteristics. These instruments typically require much more sensitive detectors to compensate for the reduced signal collected at a distance. The instrument must also have the capability to target samples at various distances with a well characterized and reproducible flux. In general, the challenges to quantitatively probing samples remotely are much more complex than with in situ instruments. The MVA techniques discussed here are applicable to both in situ and remote experiments.

The experiments presented in this paper were designed to replicate the ChemCam instrument selected for the NASA Mars Science Laboratory (MSL) rover. ChemCam includes a LIBS instrument that can probe samples up to 9 meters away from the rover mast and a Remote Micro-Imager (RMI) that will record images of the spots probed. The ChemCam LIBS instrument includes a mast unit comprised of the laser, telescope and RMI camera while the spectrometers reside in the body of the rover. The laser will produce 15 – 20 mJ/pulse onto the target samples and the laser energy depends primarily on the temperature of the laser. A single telescope is used to focus the laser into the target as well as collect the LIBS emission. An optical fiber connects the telescope to a demultiplexer (or band pass filtering unit) that directs the LIBS emission into each of three crossed Czerny-Turner spectrometers. These spectrometers are similar to the Ocean Optics HR2000 used in these experiments. For the experiments presented here, the samples were placed in a vacuum chamber filled with 7 Torr CO_2 to simulate the

martian surface atmospheric pressure. The vacuum chamber is positioned 9 meters from the collection telescope and laser.

Quantitative ChemCam LIBS analysis on Mars will present a significant challenge because different rock types with widely varying chemical compositions are expected to be present at the landing site and in its vicinity. In this paper, PLS, PCA, and SIMCA are employed to analyze remote LIBS spectra as a means of exploiting the chemical matrix effects. To simulate the anticipated geological diversity, the present study was undertaken on a set of igneous and highly metamorphosed rock samples with major and minor element concentrations that cover ranges found in typical commonly-occurring rock types (Table 1). The Total Alkali Silica (TAS) classification of these 18 samples is depicted in Fig. 1 to demonstrate the geological diversity of these samples. [25] The resultant compositional variability (Table 2) should exacerbate chemical matrix effects and provide a challenging test of the MVA techniques. PLS is employed to create a calibration model that accurately predicts the elemental composition of the unknown samples. Cluster analysis was undertaken with PCA as a means to extract information about chemical similarities among samples that may provide keys to rock identifications in unknown samples. Finally, several PCA models were generated and Soft Independent Modeling of Class Analogy (SIMCA) was employed to predict the rock-types of a subset of LIBS spectra treated as unknowns.

2. Experimental

2.1 Sample Selection, Preparation and Independent Quantitative Analysis

The 18 samples probed in this study were analyzed in the XRF lab at the University of Massachusetts (under the direction of Michael J. Rhodes) using standard operating

procedures.[26, 27] About 150 g of each sample were crushed to <45 μm particle size in a Spex tungsten carbide shatterbox. Aliquots of this powder were used for both XRF and LIBS.

For the XRF analysis of major elements, samples were prepared as fused La-bearing lithium borate glass discs using a modification of the methods of Norrish and Hutton (1969)[28], though each sample was first ignited at 1000 °C for several hours in order to oxidize the iron to Fe^{3+} and remove volatiles. All elements (including Na_2O) were measured simultaneously using a Siemens MRS-400 spectrometer. Intensities were corrected for nonlinear background, inter-element interferences, and variations in mass absorption coefficient, using methods modified from those of Norrish and Chappell (1967).[29] Mass absorption coefficients for elements with shorter characteristic wavelength than the Fe-absorption edge were estimated from the intensity of the Compton radiation of the appropriate X-ray tube.[30] Mass absorption coefficients of elements with longer characteristic radiation than the Fe absorption edge were calculated from the Compton-derived mass absorption coefficients, after allowance was made for Fe and Ti intensities.[31] Estimates of the accuracy and precision are given in Rhodes. [32]

The LIBS samples were prepared from splits of the same materials used in the XRF analysis discussed above. The samples were powdered to <45 μm grain size, an order of magnitude smaller than the LIBS beam size, and pressed into pellets. To form the pellets, 3.5 g of sample were poured into a sleeve inside a 30 mm die. Then the sleeve was carefully removed and an over-full teaspoon of boric acid was poured around the sample to form a protective casing around the pellet. The samples were not mixed with boric acid nor were any binders added. The plunger was then inserted and 5 tons of pressure were applied for a few seconds. The resultant total pellet depth is ~1.15-1.3 mm and the sample depth in the pellet is ~0.5 mm, which was

sufficiently thick that no signal from the boric acid protective casing was detected in the rock analyses.

2.2 Remote LIBS Experimental Methods

The experimental parameters were selected to replicate those of the ChemCam LIBS instrument as closely as possible. Some of the ChemCam instrumental details have been discussed in detail elsewhere.[33-35] This section includes a detailed description of the current laboratory experimental design with emphasis on the differences between the laboratory setup and the current ChemCam design (Table 3). A Spectra-Physics Indi Nd:YAG laser operating at 1064nm, 10 Hz repetition rate, and a 10ns pulse width was focused onto the samples. In these experiments, the laser energy was reduced to 17 ± 1mJ/pulse to closely replicate the on-target energy produced by the ChemCam laser. The laser was directed through a telescope that reduces the laser beam diameter before it is directed through a Newport 10x beam expander. The beam expander focuses the laser onto the sample surface positioned 9 m away from the beam expander; the telescope used to collect some of the plasma emission. A Spiricon Scor-20 camera was used to measure the $1/e^2$ diameter of 490 ± 10μm to replicate the expected ChemCam spot size at 9 m.

The samples were placed in a vacuum chamber and filled with approximately 7 Torr CO_2 to simulate the martian atmosphere. A 12″ extension tube was added to the vacuum chamber to move the window away from the sample and the dust created by the sample ablation. The CO_2 was injected into the vacuum chamber through a port on the extension such that the continuous flow of CO_2 from the flange to the pumping port on the opposite side of the vacuum chamber would further reduced the accumulation of material on the window. The vacuum chamber holds

12 samples at one time so the 18 samples were probed in two sets. Three of the samples (granophyric dike, WMG and 1984Aa) were randomly selected for inclusion in both sets in order to verify that the experimental setup remained constant.

Some of the plasma emission was collected with a Questar Field Model Telescope with an 89 mm aperture that is smaller than the 110 mm telescope on ChemCam. The standard BK7 optics within the Questar telescope were replaced with fused silica such that the UV spectrum down to ~220nm was collected. The collected emission was directed into a 1 m, 300μm, 0.22NA, Ocean Optics Solarization Resistant fiber. The fiber was connected to one of three Ocean Optics HR2000 spectrometers, each covering a different spectral region including 223.40 – 325.97 nm (UV spectrometer), 381.86 – 471.03 nm (VIS spectrometer) and 494.93 – 927.06 nm (VNIR spectrometer). The spectral resolutions for the UV, VIS, and VNIR spectrometers are 0.1, 0.09, and 0.42 nm full-width half-maximum, respectively.

The Ocean Optics Spectrometers used in these experiments are commercial instruments that use Sony CCD detectors that are limited by read-out noise rather than dark noise, even for exposures of 2 seconds. Consequently, greater signal-to-noise levels are obtained when the integration time is increased to monitor several laser shots. By contrast the ChemCam spectrometers employ more sensitive e2V detectors with single shot exposures.

For the present experiments, the integration time was set to one second, during which ten spectra were normally recorded. For each sample, five such exposures were recorded without interruption while the sample was moved slightly to expose a fresh analysis spot for each exposure. The drawback of optimizing the signal-to-noise with multiple shots per read is that the laser is not triggered at the start of each exposure. The emission from an extra laser pulse (11 shots per exposure rather than 10 shots) was occasionally observed. However, this extra laser

shot only produces a two percent increase in signal for each sample measurement consisting normally of 50 consecutive laser shots. The spectra normalization procedure discussed in section 3.1 below compensates for this error.

3. Results and Discussion

The 104 LIBS spectra (90 plus some duplicates to ensure uniform sample conditions in the chamber from one group of samples to another) from the 18 samples were processed using two approaches. Conventional univariate analysis was completed in which diagnostic peak areas were calculated. These results yielded calibration curves with relatively poor statistics, and will largely be discussed in a companion paper (in preparation). A new MVA approach to calibrate and quantitatively analyze the spectra will be described in this section. Both processes begin with normalization of the spectra to reduce the spectral fluctuations. Finally, the PLS, PCA, and SIMCA are discussed and demonstrated.

3.1. LIBS Spectra and Spectral Normalization

Fig. 2 shows the LIBS spectra for three of the 18 samples studied. . The spectra depicted in Fig. 2 are averages of the five exposures from each sample. LIBS spectra tend to be structurally complex, containing multiple emission lines for most of the elements in the sample. Some of the stronger elemental emission lines are identified in the spectra in Fig. 2. The three spectra in Fig. 2 show the complete range of SiO_2 concentrations, where WMG (bottom spectrum) has the lowest concentration, VH-1 (top spectrum) has the highest concentration and BK-2 (middle spectrum) has a concentration roughly halfway between these extremes. The differences in SiO_2 concentration are obvious upon inspection of the UV spectra (top set of

spectra in Fig. 2). The strongest Si emission line is the 288.16nm (^{1}D - ^{1}P° transition[36]) as identified in the spectra. The relative magnitude of the VH-1 Si emission line is clearly the largest and the BK-2 Si emission line is larger than WMG with the lowest concentration. The same trend is also observed for the Na concentration at 589.59 nm (^{2}S – ^{2}P° transition, bottom set of spectra).[36] All of the other 101 spectra from the other 15 samples not pictured have similarly complex spectral structures.

The averaged spectra were normalized to the total emission intensity. Many laboratory laser-based measurements involve normalizing the spectra to the total emission intensity measured by a separate non-dispersive detector. However, ChemCam will not include a separate total emission detector for normalization. Alternatively, the total emission intensity for each spectral channel (UV, VIS, and VNIR) can be calculated from the total integrated intensity.[10, 12] Each spectral channel is normalized independently by dividing each wavelength pixel by the total integrated intensity for that spectral channel. After the spectra from each spectral channel were normalized, they were compiled into a single file for MVA.

3.2. Atomic Fraction vs. Weight Percent

Because oxide weight percents are the accepted reporting notation for geological samples, all tables and figures in this paper are in weight percents. In oxide weight percent notation each major element is paired with the number of oxygen atoms needed for charge balance, in keeping with conventional geochemical analysis methods such as the X-ray fluorescence technique used for independent analyses of our samples. For example, Mg_2SiO_4 is deconvolved into MgO and SiO_2. This convention is a historical artifact of the original wet-chemical techniques used in rock and mineral analysis. However, techniques such as LIBS

physically respond to the atomic fraction stoichiometrically of a given element, not its oxide weight percent, and the two are not equivalent. Aucélio et al. used LIBS to study a relatively simple system of copper in a graphite and aluminum matrix and found that the Cu calibration was linear with mole percent and exponential-like with weight percent.[37] Mole percent is equivalent to mole fraction and atomic fraction (when multiplied by Avogadro's number, N_A) As an example of the difference within a set of geological samples, the olivine mineral group usually occurs with composition along the solid solution between two end-members: forsterite (Mg_2SiO_4) and fayalite ($Fe^{2+}{}_2SiO_4$). It is apparent from the formula that the atomic fraction of Si and O is the same regardless of which end-member cation is present. However, because Mg and Fe differ substantially in their atomic mass, the weight percent of SiO_2 differs between the two end-members, as shown in Table 4. A calibration curve using oxide weight percents of fayalite and forsterite would show differing amounts of SiO_2, even though the two should respond with similar Si and O emission line intensities. Accordingly, it is important that geological standards be converted to atomic fractions before fitting calibration curves.

3.3. Partial Least Squares (PLS)

MVA is one of many advanced analytical tools used in the field of chemometrics, which generally involves the development of mathematical or statistical models to analyze complex chemical data. In the current application, the LIBS spectra are the *X (independent)* variables and the elemental compositions are the *Y (dependent)* variables. The PLS analysis involves generating a regression model that correlates the two matrices, the LIBS spectra (**X**) and the elemental concentrations (**Y**) as described by equation 1.[17, 18, 38]

$$\mathbf{Y} = \mathbf{X}\,\mathbf{B} \qquad (1)$$

Equation 1 is a very simplified representation of the model and these matrices are typically compressed.[17, 18, 38] The **X** matrix (samples × total pixels in all channels) includes the intensity of each channel (the measurable) for each calibration sample. The **Y** matrix (samples × elemental atomic fractions) contains the elemental concentrations for each element (the responses) in each calibration sample. The **B** matrix describes the relationship between the pixel intensities and the elemental response. There are two types of PLS analysis. PLS1 involves only one *Y* variable and PLS2 involves the simultaneous analysis of multiple *Y* variables.[17-19, 38]

All of the LIBS spectra in this paper were analyzed with PLS2 where all of the elements listed in Table 2 were simultaneously analyzed. Generation of the calibration model involves a PLS2 analysis in which the elemental concentrations are known and the model is used to predict the concentrations of unknowns. There are many commercial and freeware programs available to analyze various complex, multidimensional analytical observations. The analysis presented here employed the Unscrambler program. A more detailed description of mathematical models used in the Unscrambler can be found in Martens and Naes.[18]

The PLS analysis generates a regression plot similar to Fig. 3 for each element (dependent variable) in the model and Fig. 3 contains a regression plot for Si as an example. The analysis determines the statistical correlation between the elemental variations and the observed variations in each pixel. The resulting regression analysis produces the b-coefficients for each channel and each element that is a measure of the correlation described in **B**. These regression plots contain all the information needed to predict the concentration of an unknown sample and thus are the new "calibration curves."

The model does not include any information regarding the specific wavelength for each spectral data point, nor is the model programmed with the typical emission lines used to calibrate

each individual element. As shown in Fig. 3, PLS does identify a correlation with the typical Si emission lines at 288nm, 250.69 – 252.9nm, as well as the weaker Si emission lines at 634.7 and 637.1nm as depicted in the inserted spectrum. It is also interesting to note that PLS identifies correlations with many of the emission lines associated with other elements in the matrix at specific electronic and ionization states. Because the model employs the elemental atomic fractions, as the concentration of one element increases (such as Si), one or more other elements must decrease. The broad distribution of sample chemistries included in this study involves complex atomic fraction changes in multiple elements and consequently much more significant influence in the chemical matrix. Regression plots are used to identify correlations between the element of interest (e.g., Si in Fig. 3) and the remaining matrix.

Finally, the PLS analysis employs a linear combination of values to correlate the spectral changes with the elemental compositions as follows:

$$Y = b_0 + b_1 X_1 + ...b_k X_k + e\,. \qquad (2)$$

In Equation 2, Y is the elemental composition, X_n is the spectra channel and b_n is the regression coefficient and e is the error matrix.[17, 18, 38] Fig. 3 contains the Si regression plot for 18 samples and 104 individual spectra. The PLS analysis included a full cross-validation in which each spectrum was removed from the model and treated as an unknown. The analysis generated a model with the remaining spectra and the elemental composition of the unknown is calculated. This process is repeated as each spectrum in the model is successively removed from the training set. This produces the most rigorous PLS model and requires the most CPU time. Fig. 4 contains the validation plots for eight of the ten elements analyzed. These validation plots demonstrate the close correlation between the model (black symbols) and the predicted values of the samples removed in the cross validation analysis (open symbols).

The fact that the regression model can identify elemental emission lines for the elements present in the sample can also be misleading. A preliminary assessment of the unknown spectra must be completed to identify which elements are present. If the unknown sample does not contain some of the elements present in the calibration samples, PLS can erroneously find and calculate concentrations for species in the calibration model that are clearly not in the unknown. For example, the PLS calibration model generated with the 18 igneous samples discussed in this paper could be used to quantitatively analyze an elementally less complex sample such as fayalite (Fe_2SiO_4) or quartz (SiO_2). The PLS model generated will also likely predict concentrations for the other major elements obviously not present in the unknown samples such as Ca, Mg and K. Typically (but not always), the predicted concentration for an element not present in the sample is obviously wrong and the reported concentration is a negative number or the predicted uncertainty is significantly larger than the predicted value. It is simply easier to first qualitatively assess which elements are present and then reject the predicted concentrations of those not present. Ideally, the model would be instructed to only analyze those elements present in the sample based on the signature emission lines present. However, the Unscrambler software used here does not allow creation of a model for all of the major elements that can predict only a subset of the elements. Another, different model could be generated using fewer elements but this would require many additional hours of computer time.

On the other hand, the PLS analysis will only identify elements that are already present in the calibration data set. For example, the suite of igneous rocks assembled for the present study has not yet been analyzed for carbon. Therefore, the calibration model generated with this suite of calibration samples would not be capable of quantitatively determining the carbon concentration in carbonate rocks such as calcite or dolomite.

3.4. PLS vs. Conventional Analysis

To demonstrate the superiority of the PLS calibration described here, the same data were also analyzed with a conventional peak area analysis similar to that used in Thompson et al. [10] The spectra were normalized as discussed in section 3.1 above. Analyses for Si (288 nm) and Ca (422 nm) lines are shown in calibration curves depicted in Fig. 5. The analyses involved manually subtracting the baseline and then calculating the integrated area under each peak.

The calibration curves in Fig. 5 are typical of broadly disparate samples analyzed with LIBS. Because of the care taken to homogenize the samples, the scatter in the data is largely due to chemical matrix effects, though overlap from lines attributed to other elements may also contribute. It was clear from the intensity levels displayed in the raw LIBS spectra that the laser-to-sample coupling efficiency changed with the elemental composition. The quality of the Si calibration curve is typical of most of the elements analyzed with the univariate peak area approach.

The scatter observed in the univariate calibration curves underscores the challenge that chemical matrix effects have on calibrating LIBS spectra. Previous attempts to quantitatively analyze samples such as these would have required generating calibration curves for each rock-type. For example, Thompson et al. used a series of basalt standards to quantitatively probe two basaltic martian meteorites, DAG 476 and Zagami.[10] Similar calibration curves could have been generated for each rock-type and used to analyze the samples in this study with reasonable statistical certainty.

The PLS analysis appears to largely compensate for matrix effects, perhaps because PLS statistically identifies the changes observed in the plasma that result from the variations in the matrices. Apparently, PLS statistically identifies enough of those correlations to allow the

resulting calibration model to account for the changes in these correlations from sample-to-sample. In addition, PLS may allow information about the specific sample matrix to be extracted from analyses and efforts are underway to explore and quantify this hypothesis.

3.5. Principal Components Analysis & Soft Independent Modeling of Class Analogy

Most LIBS spectra (especially those of geological materials) are complex and contain a large amount of information in spectral features. Conventional data analysis techniques are limited to qualitative identification and calculation of elemental abundances. PCA on LIBS spectra can be employed to better describe the chemical variations in the samples and, perhaps, to extract a greater understanding of the chemical structure. The samples probed in these experiments contain elements bound to elements within a larger matrix. PCA is an effective method to reduce the redundancy in the spectral data and interpret the data relative to a subset of spectral variations.[19] The correlations extracted from PCA contain some of this matrix information. There are many excellent references that describe PCA in detail and thus the analysis is only described briefly here.[17, 18]

Fundamentally, PCA is used to identify variations in a data set. These variations are reduced to a smaller set of principal components (PC). Each PC is an abstract solution to an abstract eigenvector and the corresponding eigenvalues.[17] The first PC (PC1) contains the description of the largest variation; in other words, it accounts for more of the total variance in the data set than any of the original variables. The second PC (PC2) describes the largest remaining variation and is orthogonal to PC1.[18] This calculation continues with successively smaller descriptions of the residual variation, continuing to PC3, PC4, etc. Note that the PCA in this study uses *only* the LIBS spectra. Unlike the quantitative PLS model discussed above, PCA

does not involve any direct compositional information except for the patterns identified by the analysis in the spectra. Just as in the PLS analysis, PCA is not programmed with any wavelength information or information relating a specific LIBS emission line with a specific element.

The Unscrambler program used in the PLS analysis was also employed in the PCA. There are several variations of PCA described in the literature and the calculations discussed here involved the Non-linear Iterative Partial Least Squares (NIPALS) method. [17, 18, 38] The results of the analysis generate three sets of data, variances, loadings, and scores. Fig. 6 contains plots of the loadings for PC1 and PC2, and a plot of the scores for PC1 vs. PC2. Variances are a measure of the error in the PC and are not depicted here.

The score plot is often referred to as a PCA plot and it summarizes the variations in the samples. These plots typically involve PC1 vs. PC2, because they tend to represent most of the variations, 40% and 22% in these experiments, respectively. Each additional PC represents a smaller but significant fraction of the residual variation including PC3 = 13%, PC4 = 9%, PC5 = 6%, PC6 = 3%. Because these geological samples are elementally and spectrally complex, it is not surprising that PCs greater than two represent significant variations. We explored several 3-D plots that include PC1 vs. PC2 vs. PC3, but the distribution of data was far to complex to make any useful observations. Therefore, computational analyses that exploit more than just PC1 and PC2 will likely be instructive, such as the SIMCA analysis discussed below.

The corresponding loadings plots describe the variations that dominate each PC. The closer each peak in the loadings plot is to ±1, the more significant that peak is to the variation in the spectrum. [17, 18, 38] In these LIBS spectra, each peak can also be associated with the variations in the elements in the samples. Again, PCA is not programmed with the wavelengths associated with the emission lines for the elements.

Inspection of the loadings plots demonstrates that the PC1 variations in these samples are largely dominated by Ca and Mg where their values are generally greater than 0.2. Si and Al are also prominent in the plot with values ~0.1. PC2 is controlled by Mg, Ca, Al and Na with values generally greater than 0.1. These results demonstrate that 62% of the variation in our data set can be described by the elements that control PC1 and PC2. Several major elements, including Fe, K and O, apparently do not greatly constrain the groupings of these samples. These results contrast with those of conventional geochemical analyses. The TAS classification for chemical analyses of igneous rocks [25] uses SiO_2 vs. Na_2O+K_2O (expressed in normalized wt.% oxide) contents as the basis for determining rock types.[39] However, the PCA analysis suggests that a classification system based on, perhaps, $SiO_2+Al_2O_3$ vs. $MgO+CaO+Na_2O$ (again, expressed as normalized wt.% oxides) might be a more effective means of discriminating among rock types, at least for this limited data set.

Variations of PCA have been employed in many other spectroscopic and geochemical applications. Larsen et al. employed correspondence and least squares analysis on Viking X-ray fluorescence (XRFS) and Pathfinder alpha particle x-ray spectroscopy (APXS).[40] Three different feldspar end-members were used as a training set: Ca-plagioclase, Na-plagioclase, and K-Ba feldspar. Components analysis was employed to statistically determine the relative composition each end-member had on a mixture of samples. Components analysis has subsequently been employed on Mars Exploration rover observations as well.[41, 42]

Similar analysis techniques will be extremely valuable for ChemCam LIBS analysis. LIBS probes very small spots on each sample ranging from 100-500 μm. The LIBS analysis of the martian meteorites DAG 476 and Zagami in Thompson et al. clearly probed grain boundaries and the resulting elemental composition was a mixture of end-members (c.f. refer to Fig. 7 of

Thompson et al).[10] The Al_2O_3 composition from the DAG 476 LIBS analysis was 17.5% higher than the bulk analysis reported by other sources. It was speculated that none of the relatively large olivine grains (essentially free of Al) was probed with LIBS and that this increased the deviation.

The PCA plot in Fig. 6 demonstrates that various samples and in some cases rock types may be clustered and distinguished. For example, the PC1 and PC2 scores for the basalts (1984Aa and Moppin), trachyandesites (BK-2 and Atascosa), basaltic andesites (BWQC-1 and BWQF-1) as well as two of the five dacites (Pipe Creek and Tronj) are all similar. Because PCA is a more complicated and comprehensive view of the rock types, there were a few samples that were not clustered well: primarily, the three remaining dacitic compositions (ultramafic, WMG, and VH-49). Furthermore, there is considerable overlap among the various TAS classified rock-types that makes unique identification highly speculative. This is not entirely unexpected because PC1 and PC2 only account for 66% of the variations. Consequently, a simple PCA analysis as depicted in Fig. 6 is adequate for only simple systems and a preliminary view of the samples in the model.

Soft Independent Modeling of Class Analogy (SIMCA) is another MVA classification method that employs PCA. Classification, which is not the same as clustering, is a method by which new samples are predictively added to existing classes of samples. The Unscrambler SIMCA analysis involves building a PCA model for each class that ideally includes enough PCs to describe most of the variations.[38] Here, a PCA model was created for each rock type for which we had one or more samples. Unknown samples are then fit or projected onto the model and a new set of loadings and scores are generated similar to those depicted in Fig. 6. Finally,

the residuals are used to determine whether the unknown fits the PCA model with a specified statistical significance.

To demonstrate the predictive capability of SIMCA, PCA models were created with the first, third and fifth LIBS spots recorded for each sample (62 LIBS spots total) and the second and fourth LIBS spots (42 LIBS spots total) were treated as unknowns. The optimal number of PCs were determined for each model and employed in the SIMCA analysis. The SIMCA classification results are summarized in Table 5. SIMCA properly classified all 42 LIBS sample spots that were removed from the calibration set and treated as unknowns. However, it incorrectly classified five of the spots from 3 samples as part of more than one class which is a success rate of 88.1%. This is consistent with the Sirven et al. observations where SIMCA and PLS-DA correct classification rate was 77.5% and 85.9%, respectively. Sirven et al improved their predictive accuracy to 100% by employing a combination of SIMCA and PLS-DA. The data here suggests that a more complete characterization of the various rock types would also improve the success rate. In this study, three of the samples were incorrectly classified as foidite. This was probably caused by the fact that only one sample was included in that rock type. The limited number of samples included in the model limited the number of PCs to one. The remaining three samples were incorrectly classified as rhyolite and basaltic trachyandesite, which included two samples each. This suggests that the training set much be increased to build more accurate and predictive PCA models for SIMCA analysis.

4. Conclusion

The ChemCam mission on MSL will involve many validation experiments performed by several members of the science team. Each laboratory will have replica calibration targets that

will be supplemented with samples required to extend the range of elements depending on the samples detected on Mars. This extended set of samples will be used to create new PLS calibration models and refine the detected elemental abundances. In cases where the rock type can be constrained to, for example, igneous rocks, the chemistries from PLS will facilitate determination of rock types based on conventional classification schemes such as the TAS classification. In situations where heterogeneous rocks, such as weathering rinds mixed with underlying rock, or sedimentary mixtures of different rocks, are analyzed, PCA may assist in constraining the relative contributions of different parent rocks. Both techniques show promise for quantitative chemical analyses of geological samples.

Acknowledgments

We gratefully acknowledge the NASA Mars Fundamental Research Program (MFRP), grant NNG06GH35G for the support of the work. We would like to thank Prof. David Brown, Prof. Ray Arvidson, Dr. Michael Ebinger and Dr. Ronny Harris for the insightful discussions regarding various multivariate analysis techniques. We also appreciate the insightful and thorough comments made by the reviewers.

References

[1] D.A. Cremers, L.J. Radziemski, Handbook of Laser-Induced Breakdown Spectroscopy, First ed., John Wiley & Sons, West Sussex, England, 2006.
[2] A.W. Miziolek, V. Palleschi, I. Schechter (Eds.), Laser Induced Breakdown Spectroscopy, Cambridge University Press, New York, 2006.
[3] V. Lazic, R. Barbini, F. Colao, R. Fantoni, A. Palucci, Spectrochim. Acta, Part B: Atom. Spectrosc. 56 (2001) 807-820.
[4] J. Vrenegor, R. Noll, V. Sturm, Spectrochim. Acta, Part B: Atom. Spectrosc. 60 (2005) 1083-1091.
[5] S.I. Gornushkin, I.B. Gornushkin, J.M. Anzano, B.W. Smith, J.D. Winefordner, Appl. Spec. 56 (2002) 433-436.

[6] A.S. Eppler, D.A. Cremers, D.D. Hickmott, M.J. Ferris, A.C. Koskelo, Appl. Spec. 50 (1996) 1175-1181.
[7] H.J. Häkkänen, J.E.I. Korppi-Tommola, Anal. Chem. 70 (1998) 4724 - 4729.
[8] C. Chaleard, P. Mauchien, N. Andre, J. Uebbing, J.-L. Lacour, C. Geertsen, J. Anal. Atom. Spec. 12 (1997) 183-188.
[9] L. Dudragne, P. Adam, J. Amouroux, Appl. Spec. 52 (1998) 1321-1327.
[10] J.R. Thompson, R.C. Wiens, J.E. Barefield, D.T. Vaniman, H.E. Newsom, S.M. Clegg, J. Geophys. Res.-Planets 111 (2006) E05006.
[11] B. Salle, J.-L. Lacour, P. Mauchien, P. Fichet, S. Maurice, G. Manhès, Spectrochim. Acta, Part B: Atom. Spectrosc. 61 (2006) 301-313.
[12] J.A. Bolger, Appl. Spec. 54 (2000) 181-189.
[13] P. Yaroshchyk, D. Body, R.J.S. Morrison, B.L. Chadwick, Spectrochim. Acta, Part B: Atom. Spectrosc. 61 (2006) 200-209.
[14] F. Colao, R. Fantoni, V. Lazic, A. Paolini, F. Fabbri, G.G. Ori, L. Marinangeli, A. Baliva, Planet. Space Sci. 52 (2004) 117-123.
[15] A. Ciucci, M. Corsi, V. Palleschi, S. Rastelli, A. Salvetti, E. Tognoni, Appl. Spec. 53 (1999) 960-964.
[16] F. Colao, R. Fantoni, V. Lazic, A. Paolini, Appl. Phys. A 79 (2004) 143-152.
[17] E.R. Malinowski, Factor Analysis in Chemistry, Third ed., John Wiley and Sons, Inc, New York, 2002.
[18] H. Martens, T. Naes, Multivariate Calibration, John Wiley & Sons, Chichester, 1991.
[19] M.Z. Martin, N. Labbe, T.G. Rials, S.D. Wullschleger, Spectrochim. Acta, Part B: Atom. Spectrosc. 60 (2005) 1179-1185.
[20] C.A. Munson, F.C. De Lucia, T. Piehler, K.L. McNesby, A.W. Miziolek, Spectrochim. Acta, Part B: Atom. Spectrosc. 60 (2005) 1217-1224.
[21] J.-B. Sirven, B. Bousquet, L. Canioni, L. Sarger, Anal. Chem. 78 (2006) 1462-1469.
[22] Z.A. Arp, D.A. Cremers, R.C. Wiens, D.M. Wayne, B. Sallé, S. Maurice, Appl. Spec. 58 (2004) 897-909.
[23] B. Salle, J.-L. Lacour, E. Vors, P. Fichet, S. Maurice, D.A. Cremers, R.C. Wiens, Spectrochim. Acta, Part B: Atom. Spectrosc. 59 (2004) 1413-1422.
[24] B. Salle, P. Mauchien, S. Maurice, Spectrochim. Acta Part B: Atom. Spectrosc. 62 (2007) 737-768.
[25] A. Streckeisen, B. Zanettin, M.J. Le Bas, B. Bonin, P. Bateman, G. Bellieni, A. Dudek, S. Efremova, J. Keller, J. Lamere, P.A. Sabine, R. Schmid, H. Sorensen, R.A. Woolley, in: R.W. Le Maitre (Ed.), Cambridge University Press, 2002.
[26] J.M. Rhodes, J. Geophys. R. 101 (1996) 11729-11746.
[27] J.M. Rhodes, M.J. Vollinger, Geochemistry, Geophysics, and Geosystems 5 (2004) Q03G13.
[28] K. Norrish, and Hutton, J.T., Geochimica et Cosmochimica Acta 33 (1969) 431-454.
[29] K. Norrish, B.W. Chappell, in: J. Zussman (Ed.), Physical Methods in Determinative Mineralogy, Academic Press, San Diego, 1967, pp. 161-214.
[30] R.C.J. Reynolds, American Mineralogist 52 (1967) 1493-1502.
[31] D. Walker, American Mineralogist 58 (1973) 1069-1072.
[32] J.M. Rhodes, Journal of Geophysical Research 93 (1988) 4453-4466.
[33] S. Maurice, R. Wiens, G. Manhes, D.A. Cremers, B.L. Barraclough, J. Bernardin, M. Bouye, A. Cros, B. Dubois, E. Durand, S. Hahn, D. Kouach, J.-L. Lacour, D. Landis, T. Moore,

L. Pares, J. Platzer, M. Saccoccio, B. Salle, R. Whitaker, ChemCam instrument for the Mars Science Laboratory (MSL) rover. Lunar Planet. Sci., Houston, TX, 2005, p. Abstract 1735.
[34] S. Maurice, R.C. Wiens, M. Saccoccio, B. Barraclough, B. Sallé, S.M. Clegg, C. team, Expected Performances of the ChemCam Instrument for the Mars Science Laboratory (MSL) Rover. Lunar Planet. Sci., Houston, TX, 2007, p. Abstract 1563.
[35] R.C. Wiens, S. Maurice, S. Clegg, D. Vaniman, J. Thompson, M.D. Dyar, E. Sklute, H. Newsom, N. Lanza, V. Sautter, J. Dubessy, M.C. Boiron, C. Fabre, J.-L. Lacour, B. Salle, P. Mauchien, D. Blaney, Y. Langevin, K. Herkenhoff, N. Bridges, G. Manhes, C. team, PREPARATION OF ONBOARD CALIBRATION TARGETS FOR THE CHEMCAM INSTRUMENTS ON THE MARS SCIENCE LABORATORY ROVER., Lunar Planet. Sci., Houston, TX, 2007, p. Abstract 1180.
[36] Y. Ralchenko, A.E. Kramida, J. Reader, NIST Atomic Spectra Database. 3.1.2 ed., 2006.
[37] R.Q. Aucélio, B.C. Castle, B.W. Smith, J.D. Winefordner, Appl. Spec. 54 (2000) 832-837.
[38] C.S. Inc, The Unscrambler. 9.7 ed., 2007.
[39] R.W. Le Maitre, A. SStreckeisen, B. Zanettin, M.J. Le Bas, B. Bonin, P. Bateman, G. Bellieni, A. Dudek, S. Efremova, J. Keller, J. Lamere, P.A. Sabine, R. Schmid, H. Sorensen, A.R. Woolley, Igneous
Rocks: A Classification and Glossary of Terms, Recommendations of the International Union of Geological Sciences, Subcommission of the Systematics of Igneous Rocks, Cambridge University Press, 2002.
[40] K.W. Larsen, R.E. Arvidson, B.L. Jolliff, B.C. Clark, J. Geophys. R. 105 (2000) 29,207-229,221.
[41] R.E. Arvidson, S.W. Squyres, R.C. Anderson, J.F. Bell, D. Blaney, J. Bruckner, N.A. Cabrol, W.M. Calvin, M.H. Carr, P.R. Christensen, B.C. Clark, L. Crumpler, D.J. Des Marais, P.A. de Souza, C. d'Uston, T. Economou, J. Farmer, W.H. Farrand, W. Folkner, M. Golombek, S. Gorevan, J.A. Grant, R. Greeley, J. Grotzinger, E. Guinness, B.C. Hahn, L. Haskin, K.E. Herkenhoff, J.A. Hurowitz, S. Hviid, J.R. Johnson, G. Klingelhofer, A.H. Knoll, G. Landis, C. Leff, M. Lemmon, R. Li, M.B. Madsen, M.C. Malin, S.M. McLennan, H.Y. McSween, D.W. Ming, J. Moersch, R.V. Morris, T. Parker, J.W. Rice, L. Richter, R. Rieder, D.S. Rodionov, C. Schroder, M. Sims, M. Smith, P. Smith, L.A. Soderblom, R. Sullivan, S.D. Thompson, N.J. Tosca, A. Wang, H. Wanke, J. Ward, T. Wdowiak, M. Wolff, A. Yen, J. Geophys. Res.-Planets 111 (2006) E02S01.
[42] R.E. Arvidson, F. Poulet, R.V. Morris, J.P. Bibring, J.F. Bell, S.W. Squyres, P.R. Christensen, G. Bellucci, B. Gondet, B.L. Ehlmann, W.H. Farrand, R.L. Fergason, M. Golombek, J.L. Griffes, J. Grotzinger, E.A. Guinness, K.E. Herkenhoff, J.R. Johnson, G. Klingelhofer, Y. Langevin, D. Ming, K. Seelos, R.J. Sullivan, J.G. Ward, S.M. Wiseman, M. Wolff, J. Geophys. Res.-Planets 111 (2006) E12S08.

Table 1
Sample Descriptions.

Samples	Description
1984 AA	1984 eruption of Mona Loa (basalt)
Atascosa	trachyandesite, Atascosa Volcanics, southern Arizona, ~23 Ma
BK-2	trachyandesite
BWQC-1	coarse-grained basaltic andesite, Westfield, MA
BWQF-1	fine-grained basaltic andesite, Westfield, MA
Cadillac	granite, Cadillac Mountain, Mt. Desert Island, Maine, 420 +/- 1 Ma
Cerro	basalt, Cerro Colorado Mountains, southern Arizona ~23 Ma
Granophyric Dike	~1700 Ma dike from Grand Canyon
Moppin	Moppin metavolcanics, metamorphosed basalt flows, 1755 Ma, northern New Mexico
MSHA	andesite, 1980 A.D., Mount Saint Helens
Pipe Creek	granitoid, mile 89.4, Grand Canyon
Red Hill	Red Hill complex, White Mountain magma series, ~198 Ma, New Hampshire, syenite
Trondjhemite	trondjhemite, ~432 Ma, near Trondheim, Norway
Ultramafic	lherzolite, mile 91, Grand Canyon, ~1700 Ma
Umphraville	syenite, near Sudbury, Ontario
VH-1	Vinalhaven granite, ~ 420 Ma, Vinalhaven, Maine
VH-49	Vinalhaven basalt, ~420 Ma, Vinalhaven, Maine
WMG	Woolen Mill metamorphosed, garnet-bearing gabbro ~1154 Ma Ma, Adirondack Mountains, New York

Table 2
Compositional Ranges for Major Elements*

Species	Minimum	Maximum	Precision**
SiO_2	43.29	76.58	0.090
TiO_2	0.09	6.22	0.005
Al_2O_3	4.04	17.46	0.028
Fe_2O_3	1.36	20.24	0.033
MnO	0.02	0.36	0.001
MgO	0.14	29.23	0.016
CaO	0.15	9.89	0.012
Na_2O	0.85	5.91	0.023
K_2O	0.39	5.60	0.002
P_2O_5	0.02	1.36	0.003

*Maximum and minimum values for the major elements as determined by XRF, given in wt. % oxide. Total iron is calculated as Fe_2O_3.

**Estimated precision for each element is taken from Rhodes (1996); these values are based on repeat analyses of KIL-1919, a Hawaii Scientific Drilling Project standard. Accuracy of each element is estimated to be comparable to precision; see Johnson et al. (1999).

Table 3
Comparison of Laboratory and ChemCam Analytical Conditions

	ChemCam	Laboratory (this study)
Laser Power on Target	15-20 mJ/pulse	17mJ/pulse
Laser Spot Size @ 9 m	489 μm*	490 ± 10 μm
Laser Pulse Width	5 ns	10 ns
Telescope Diameter	110 mm	89 mm
Optical Fiber Length and NA	6 m, 0.22	1 m, 0.22

* The ChemCam Engineering Model produced a 489um spot size at 9m. The ChemCam Flight Model now produces a ~300um spot size at 9m.

Table 4
Comparison of oxide weight percent and atomic fraction for end-members of olivine.

		Atomic Fraction			Oxide Weight Percent	
Name	Formula	Fe or Mg	Si	O	FeO or MgO	SiO_2
Fayalite	Fe_2SiO_4	0.29	0.14	0.57	70.5%	29.5%
Forsterite	Mg_2SiO_4	0.29	0.14	0.57	57.3%	42.7%

Table 5
TAS Classification predictions by SIMCA.

Sample	TAS Classification	SIMCA Prediction
MSHA (1)	basaltic trachyandesite	basaltic trachyandesite
MSHA (2)	basaltic trachyandesite	basaltic trachyandesite
Trondjhemite (1)	dacite	dacite
Trondjhemite (2)	dacite	dacite
VH-1 (1)	trachyte	trachyte
VH-1 (2)	trachyte	trachyte
Moppin (1)	basalt	basalt
Moppin (2)	basalt	basalt
Ultramafic (1)	dacite	dacite
Ultramafic (2)	dacite	dacite
Granophyric Dike (1)	basaltic trachyandesite	basaltic trachy ndesite
Granophyric Dike (2)	basaltic trachyandesite	basaltic trachyandesite
1984AA (1)	basalt	basalt
1984AA (2)	basalt	basalt
WMG (1)	dacite	dacite
WMG (2)	dacite	dacite
BK-2 (1)	trachyandesite	trachyandesite
BK-2 (2)	trachyandesite	trachyandesite
Umphraville (1)	foidite	foidite
Umphraville (2)	foidite	foidite
BWQF-1 (1)	basaltic andesite	basaltic andesite
BWQF-1 (2)	basaltic andesite	basaltic andesite
PipeCreek (1)	**dacite**	**dacite, foidite**
PipeCreek (2)	**dacite**	**dacite, foidite**
RedHill (1)	rhyolite	rhyolite
RedHill (2)	rhyolite	rhyolite
VH-49 (1)	dacite	dacite
VH-49 (2)	dacite	dacite
Cadillac (1)	basaltic trachyandesite	basaltic trachyandesite
Cadillac (2)	basaltic trachyandesite	basaltic trachyandesite
BWQC-1 (1)	basaltic andesite	basaltic andesite
BWQC-1 (2)	basaltic andesite	basaltic andesite
Cerro (1)	rhyolite	rhyolite
Cerro (2)	rhyolite	rhyolite
Atascosa (1)	**trachyandesite**	**trachy andesite, rhyolite**
Atascosa (2)	**trachyandesite**	**trachy andesite, basaltic trachyandesite, foidite, rhyolite**
Granophyric Dike (1)	basaltic trachyandesite	basaltic trachyandesite
Granophyric Dike (2)	basaltic trachyandesite	basaltic trachyandesite
WMG (1)	dacite	dacite
WMG (2)	dacite	dacite
1984AA (1)	**basalt**	**basalt, basaltic trachyandesite**
1984AA (2)	basalt	basalt

The samples in bold were the only samples that classified the unknowns as part of more than one rock-type. *The Woolen Mill sample is a metamorphic rock, but it is treated as an igneous rock on the basis of chemistry here for demonstration purposes.

Figure Captions

Fig. 1. Igneous rock classification for the 18 samples in this study, using chemical analyses from XRF and the TAS classification system.[39] Note that the WMG sample is a metamorphosed gabbro, but its composition is shown on this plot to indicate where it would fall if it was igneous.

Fig. 2. Three representative LIBS spectra for VH-1, BK-2, and WMG that were selected based on their relative SiO_2 oxide weight percent. The LIBS spectra from all 18 samples were similarly complex, including emission lines for all of the major elements explored in this study.

Fig. 3. The regression coefficients generated with PLS2 for Si. Note that the PLS method successfully identified the typical Si emission lines observed at 250.69 – 252.9 nm, 288 nm, 634.7 nm and 637.1 nm. Similar regression plots were prepared for all of the elements included in this study.

Fig. 4. Model and validation plots produced with PLS2 in which the known vs. PLS predicted oxide weight percents are displayed. The solid black circles and solid line represent the model while the open circles and dashed line represent the resulting validation. For each sample probed, the model and validation data points were averaged and the error bars in the plot represent the standard deviation. Note that the Ti model and validation plots are not included and are similar to the other elements presented here.

Fig. 5. Representative calibration curves generated by the integrated peak area vs. elemental atomic fraction for Si (288 nm) and Ca (422 nm). There are 21 data points in these plots. These experiments were completed in two sets and three of the samples were included in both sets.

Fig. 6. (Top) The PCA plot containing the PC1 vs. PC2 scores for all five spectra for all 18 samples probed. (Bottom) The loadings plots for PC1 and PC2 that demonstrate which elements and emission lines describe the variations included in PC1 and PC2.

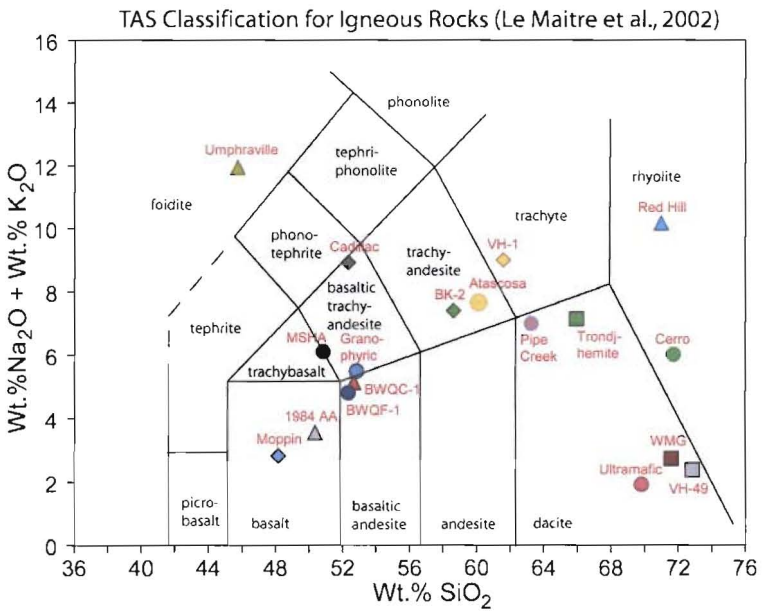

Clegg et al. Fig. 1

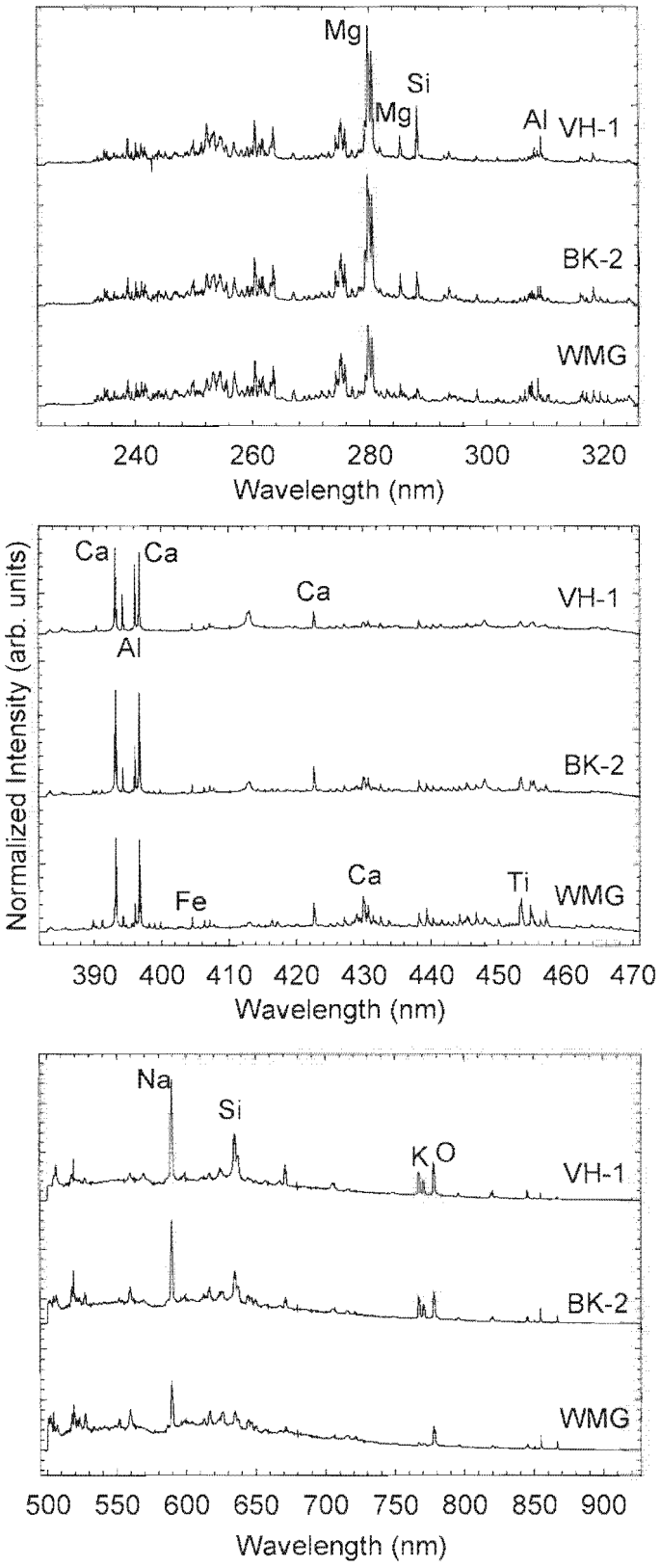

Clegg et al. Fig. 2

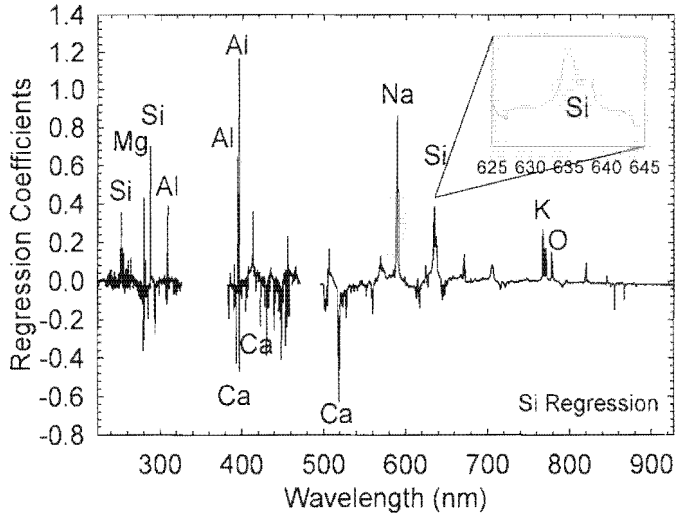

Clegg et al. Fig. 3

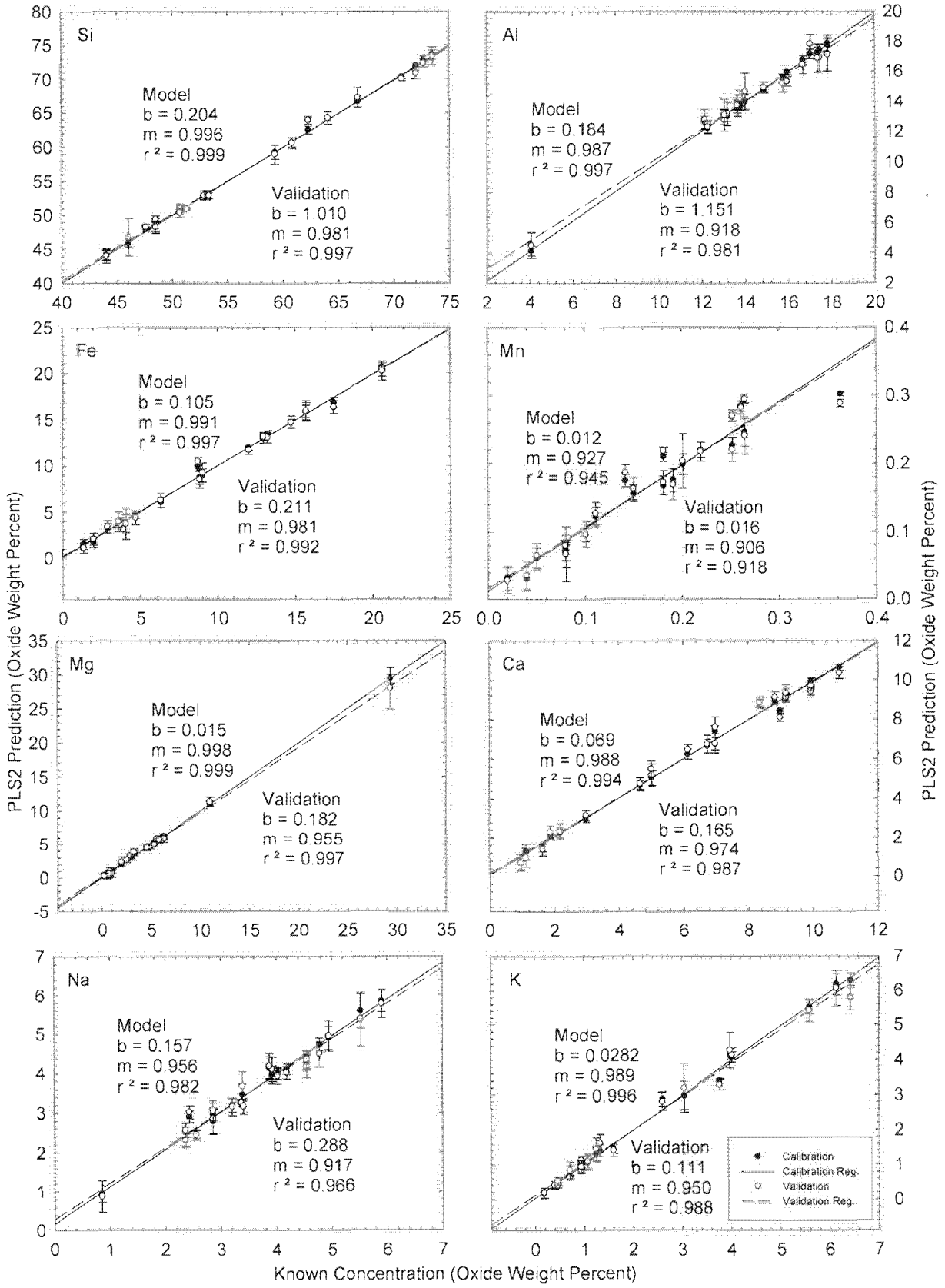

Clegg et al. Fig. 4

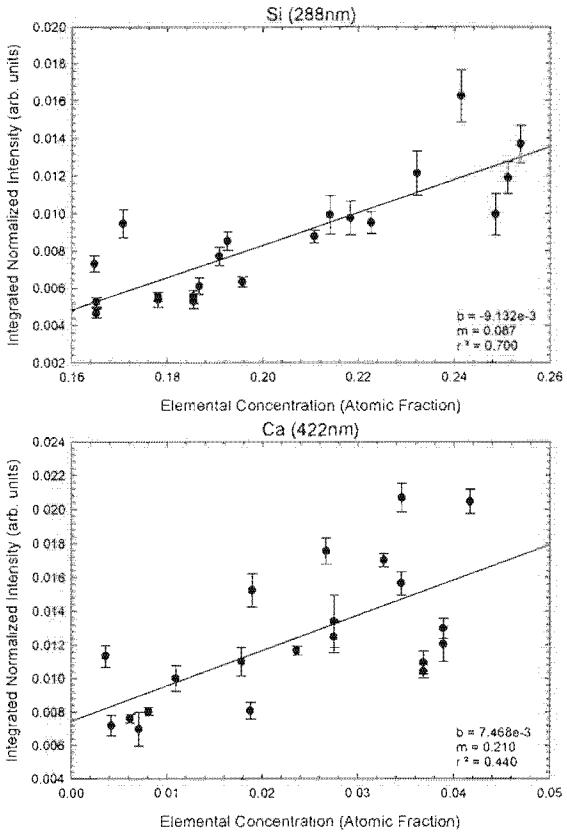

Clegg et al. Fig. 5

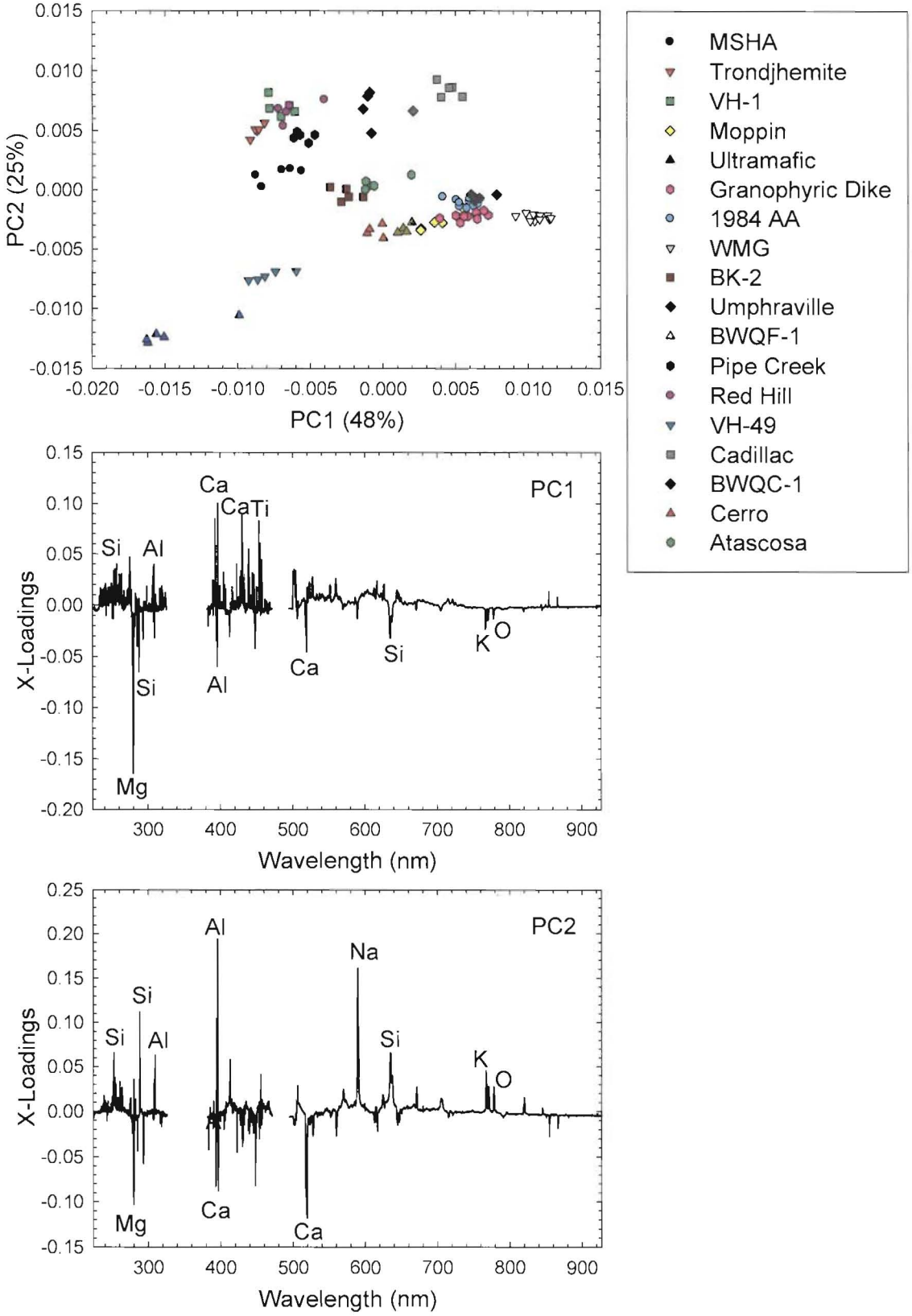

Clegg et al. Fig. 6